Available online at www.sciencedirect.com
ScienceDirect
Journal of Computational Physics 220 (2006) 139–154
JOURNAL OF COMPUTATIONAL PHYSICS
www.elsevier.com/locate/jcp

Rheology of red blood cell aggregation by computer simulation

Yaling Liu, Wing Kam Liu *

Department of Mechanical Engineering, 2145 Sheridan Road, Northwestern University, Evanston, IL 60208, United States

Received 7 August 2005; received in revised form 21 February 2006; accepted 5 May 2006
Available online 30 June 2006

Abstract

The aggregation of red blood cells (RBC) induced by the interactions between RBCs is a dominant factor of the in vitro rheological properties of blood, and existing models of blood do not contain full cellular information. In this work, we introduce a new three-dimensional model that couples Navier–Stokes equations with cell interactions to investigate RBC aggregation and its effect on blood rheology. It consists of a depletion mediated aggregation model to describe the interactions of RBCs and an immersed continuum model to track the deformation/motion of RBCs in blood plasma. To overcome the large deformation of RBCs, the meshfree method is used to model the RBCs. Three important phenomena in blood rheology are successfully captured and studied via this approach: the shear rate dependence of blood viscosity, the influence of cell rigidity on blood viscosity, and the Fahraeus–Lindqvist effect. As a microscopic illustration of the shear-rate dependence of the blood's viscoelasticity, the disaggregation of an RBC rouleau at shear rates varying between 0.125 and 24 s^{-1} is modeled. Lower RBC deformability and higher shear rates above 0.5 s^{-1} are found to facilitate disaggregation. The effective viscosities at different shear rates and for cells with different deformabilities are simulated. The numerical results are shown to agree with the reported experimental measurements. The Fahraeus–Lindqvist effect is, for the first time, studied through three-dimensional numerical simulations of blood flow through tubes with different diameters and is shown to be directly linked to axial-migration of deformable cells. This study shows that cell–cell interaction and cell deformability have significant effects on blood rheology in capillaries.

Keywords: Immersed finite element method; Navier–Stokes equations; Cell interaction; Red blood cell; Aggregation; Hemorheology; Capillary

1. Introduction

The aggregation of human red blood cells (RBC) is a dominant factor of the in vitro rheological properties of blood. Past studies on RBC aggregation [1–3] have confirmed the effects of fibrinogen (a cross-linking protein) concentration on RBC aggregation. Due to the presence of fibrinogen on cell membranes and globulin in the plasma, RBCs tend to form aggregates called rouleaus, in which RBCs adhere loosely like a stack of coins. The presence of massive rouleaus can impair the blood flow through micro- and capillary vessels and cause

* Corresponding author. Tel.: +1 847 491 7094; fax: +1 847 491 3915.
E-mail address: w-liu@northwestern.edu (W.K. Liu).

0021-9991/$ - see front matter © 2006 Elsevier Inc. All rights reserved.
doi:10.1016/j.jcp.2006.05.010

fatigue and shortness of breath. The difference in the percentage of aggregated RBCs may be an indication of a thrombotic disease. Recently, Neu and Meiselman [4] proposed a theory for depletion mediated RBC aggregation. However, the direct link between RBC aggregation and the rheological properties of blood has not been established yet. It is therefore of significant clinical relevance to understand blood composition and its rheological behavior in the context of multiscale and multiphysics hemodynamics. In this paper, the macroscopic rheological properties of the blood will be shown to be determined by the cellular scale nature of blood cells.

Human blood is a biological fluid composed of deformable cells, proteins, platelets, and plasma. In the study of the heart, arteries, and veins, blood is usually simplified as a homogeneous Newtonian fluid. However, the rheological behavior of blood flows in micro- and capillary vessel strongly depends on the flow condition, cell deformability, vessel size, and many other biochemical factors [5,6]. Biological phenomena such as blood coagulation, sickle cell disease, involve the cellular and molecular nature of blood. Eggleton and Popel [7] have studied deformation of one or two cells under shear flow. Wagner et al. [8,9] have modeled the shear flow with rigid particles with continuum enrichment methods. However, no method is yet available to study blood rheology in micro-vessels from the underlying cellular mechanism. Currently, there are three critical challenges in direct numerical simulation of the blood flow with deformable RBCs: the coupling between complex nonlinear solid motions and fluid flow, handling very large deformation of solids, and computational expense.

In [10], we have presented a two-dimensional model of blood cell interactions. Due to the difficulties in handling large RBC deformations and the limitations of 2D simulation, only simple illustrative examples of cell–cell interactions were given there. In this work, we concentrate on the rheological aspects of three-dimensional flow systems of micro- and capillary vessels which involve deformable cells, cell–cell interactions, and complex flow conditions. In particular, we propose a new modeling technique which combines the newly developed immersed finite element method (IFEM) [11,33] with RBC–RBC interaction mechanisms. It consists of a depletion mediated aggregation model introduced by Neu and Meiselman [4] to describe the interactions of RBCs and an immersed continuum model to track the deformation/motion of RBCs in plasma. We have used a meshfree formulation [28] to handle the large deformation of RBCs. Our results suggest that cell interaction and cell deformability are critical factors that influence the hemorheology in capillaries.

We first describe the discrete RBC model and aggregation model, and illustrate the key ingredients of the proposed combination of the IFEM and cell interactions. The results are then presented in Section 3, where the shear rate dependent blood viscosity, the influence of cell rigidity, and the Fahraeus–Lindqvist effect are studied. The conclusions are presented in Section 4.

2. Method

2.1. Discrete RBC model

In suspension culture, RBC assumes a biconcave disc shape which permits its passage through capillaries and enables its surface to volume ratio to be significantly higher than that of a sphere. In addition, the biconcave disc shape suggests that the membrane cytoskeleton has both bending and membrane rigidities. The RBC membrane is modeled as a flexible three-dimensional thin structure enclosing an incompressible fluid, using a Lagrangian description. Both the cytoplasm inside the RBC and the blood plasma outside the RBC have a viscosity of around 0.01 dyn s/cm, thus are treated as the same fluid.

The static shape of a normal RBC is a biconcave discoid. The x–y coordinates of the cross-sectional profile of a RBC are described by

$$\bar{y} = 0.5[1 - \bar{x}^2]^{1/2}(a_0 + a_1\bar{x}^2 + a_2\bar{x}^4), \quad -1 \leqslant \bar{x} \leqslant 1 \tag{1}$$

with $a_0 = 0.207$, $a_1 = 2.002$, and $a_2 = 1.122$, and the non-dimensional coordinates $\bar{x}$ and $\bar{y}$ are scaled as $x/5$ μm and $y/5$ μm, respectively.

A Mooney–Rivlin strain energy function is used to depict the material behavior of the RBC membrane

$$W = C_1(I_1 - 3) + C_2(I_2 - 3) \tag{2}$$

with the material properties specified by constants C_1 and C_2. I_1 and I_2 are the functions of the invariants of the Cauchy–Green deformation tensor $\mathbf{C}$ defined as $C_{ij} = F_{mi}F_{mj}$, where $F_{ij} = \partial x_i/\partial X_j$ is the deformation gradient. $I_1 = C_{ii}$ and $I_2 = \frac{1}{2}(C_{ii}C_{jj} - C_{ij}C_{ji})$. The Mooney–Rivlin or Neo-Hookean strain energy is also adopted by Skalak et al. [12], Eggleton and Popel [7] and Pozrikidis [13] in RBC deformation modeling. Following [12], $C_1 = 2.57 \times 10^6$ dyn/cm^2 and $C_2 = 0.257 \times 10^6$ dyn/cm^2 are used, which is equivalent to a Young modulus of 10^7 dyn/cm^2. It should be mentioned that different constitutive laws can be easily applied for different membrane material properties. This is important when considering sickle cells, which are stiffer than normal RBCs.

2.2. RBC aggregation model

It is well-known that RBCs tend to form rouleaus due to cell interactions. The formation of such rouleaus depend on the initial position of the cells, the strength of the adhesive force, elastic forces, and hydrodynamic forces. From the theory of adhesion of two elastic bodies, Skalak et al. [14] gave a general dynamic equation of rouleau formation based on energy conservation

$$\frac{\mathrm{d}U}{\mathrm{d}t} = \frac{\mathrm{d}W}{\mathrm{d}t} + \frac{\mathrm{d}T}{\mathrm{d}t} + \frac{\mathrm{d}D}{\mathrm{d}t} - \phi\frac{\mathrm{d}A_\mathrm{c}}{\mathrm{d}t}, \tag{3}$$

where $\frac{\mathrm{d}U}{\mathrm{d}t}$ is the rate of work done by the external forces, $\frac{\mathrm{d}W}{\mathrm{d}t}$ is the rate of increase of elastic energy, $\frac{\mathrm{d}T}{\mathrm{d}t}$ is the rate of change of kinetic energy, $\frac{\mathrm{d}D}{\mathrm{d}t}$ is the rate of dissipation of energy (energy dissipated in the viscous fluid) and $-\phi\frac{\mathrm{d}A_\mathrm{c}}{\mathrm{d}t}$ is the rate of supplied force to separate the contact surfaces. The interaction energy ϕ is defined by

$$\phi = \int_{y_0}^{\infty} \sigma_\mathrm{n}\,\mathrm{d}y = \int_{y_0}^{\infty}\int_{\Omega} f\,\mathrm{d}\Omega\,\mathrm{d}y, \tag{4}$$

where σ_n is the net force between two opposing membrane surfaces, y_0 is the equilibrium spacing, Ω is the surface area of the opposing membrane and f is the molecular level interaction force.

However, in [14], Eq. (4) is not evaluated directly due to the lack of the interaction forces at a molecular level. Also, only steady static cases are considered, thus the kinetic energy, viscous dissipation, and the work done by external forces are neglected. In this paper, we fill this gap by evaluating cell–cell interaction force from molecular level while taking into account the dynamic process of RBC rouleau formation/dispersion in flow field.

Recently, Neu and Meiselman [4] proposed a theoretical model for depletion-mediated RBC aggregation in polymer solutions. In their derivation, the total interaction energy ϕ per unit area of cell surface is given by the summation of the depletion interaction energy w_D and the electrostatic interaction energy w_E as

$$\phi = w_\mathrm{D} + w_\mathrm{E}. \tag{5}$$

Given a depletion layer thickness Δ and a separation distance of r between adjacent surfaces, w_D is given by the osmotic pressure and depletion layer thickness as

$$w_\mathrm{D} = -2\Pi\left(\Delta - \frac{r}{2} + \delta - p\right), \tag{6}$$

where the osmotic pressure term $\Pi = -\frac{(\mu_1 - \mu_1^0)}{v_1}$ (v_1 is the molecular volume of the solvent, μ_1 and μ_1^0 are the chemical potential of the solvent in the polymer solution and in polymer free solution separately), δ indicates the thickness of the attached polymer layer, and p is the penetration depth of the free polymer into the attached layer.

The electrostatic free energy of two cells is calculated by the integration of electric charges as

$$E = \frac{1}{2}\int_0^r \int_0^\mathrm{p} \psi(\rho, x)\,\mathrm{d}\rho\,\mathrm{d}x \tag{7}$$

in which ψ is the electrostatic potential between the cells, which depends on the charge density ρ and x

The integration of the electrostatic free energy finally gives

$$w_\mathrm{E} = \frac{\sigma^2}{\delta^2\varepsilon\varepsilon_0\kappa^3}\begin{cases} \sinh(\kappa\delta)(\mathrm{e}^{\kappa\delta-\kappa d} - \mathrm{e}^{-\kappa d}) & d \geqslant 2\delta, \\ (2\kappa\delta - \kappa d) - (\mathrm{e}^{-\kappa\delta} + 1)\sinh(\kappa\delta - \kappa d) - \sinh(\kappa\delta)\mathrm{e}^{-\kappa d} & d < 2\delta, \end{cases} \tag{8}$$

where κ^{-1} is the Debye–Hückel length, ϵ and ϵ_0 are the relative permittivity of the solvent and the permittivity of vacuum.

The total interaction energy (ϕ) versus RBC–RBC separation (r) for various polymer concentrations is given by Eq. (5) and plotted in Fig. 1. The interaction energy agrees well with the experimental values of interaction energy for RBC suspended in various concentrations of DEX 70 or DEX 150 (data from [15]).

In this paper, we focus on studying the influences of RBC aggregation on viscoelastic properties of blood flows, rather than identifying the mechanism of the RBC aggregation. To simplify the total interaction energy formulation, a Morse type potential function is used to fit the curve given in Fig. 1. For example, by choosing $r_0 = 13.0$ nm, $D_e = 4.1$ μJ/m^2 and $\beta = 0.39$ nm^{-1}, we can find that such Morse type potential function fits the total interaction energy curve of 70 kDa dextran with penetration constant $c_2^p = 1$ g/dL case very well (Fig.1). Thus, the interaction forces between two RBCs can be simply modeled as the weak depletion attractive and strong electrostatic repulsive forces at far and near distances

$$\phi(r) = D_e[e^{2\beta(r_0-r)} - 2e^{\beta(r_0-r)}], \tag{9}$$

$$f(r) = -\frac{\partial\phi(r)}{\partial r} = 2D_e\beta[e^{2\beta(r_0-r)} - e^{\beta(r_0-r)}], \tag{10}$$

where r_0 and D_e stand for the zero force length and surface energy, respectively, and β is a scaling factor.

2.3. Coupling Navier–Stokes equation with cell interaction

Let us consider the RBCs as incompressible three-dimensional deformable structures in Ω^s (i.e., RBC membranes) completely immersed in an incompressible fluid domain Ω^f. Together, the fluid and the solid occupy a domain Ω exclusively. This work is based the immersed finite element method (IFEM) [11] and cell–cell interaction model.

The immersed finite element method [11] is developed by merging the concept of immersed boundary (IB) [16,17], finite element, and meshfree methods for nonlinear fluids and solids. In IFEM, independent solid meshes may be thought of moving on top of a fixed background fluid mesh. This simple strategy removes the expensive mesh-update cost and enables an efficient coupling of immersed RBCs with the surrounding viscous fluid. In the computation, the fluid spans the entire domain Ω, thus an Eulerian fluid mesh is adopted; a Lagrangian solid mesh is constructed on top of the Eulerian fluid mesh.

In the computational fluid domain Ω, the fluid grid is represented by the time-invariant position vector $\mathbf{x}$; while the material points of the structure in the initial solid domain Ω_0^s and the current solid domain Ω^s are

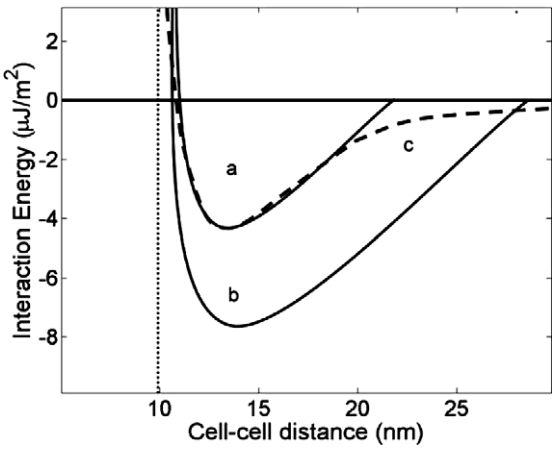

Fig. 1. Total interactional energy (ϕ) versus RBC–RBC separation (r) for various values penetration constant (defined as c_2^p in [4]) for cells in 70 kDa dextran. (a) $c_2^p = 1$ g/dL, (b) $c_2^p = 10$ g/dL, (c) fitted curve by a Morse potential described in Eq. (9). The dashed vertical line at 10 nm indicates the total glycocalyx thickness for both cells. Reproduced from [4].

represented by $\mathbf{X}^s$ and $\mathbf{x}^s(\mathbf{X}^s, t)$, respectively. The superscript 's' corresponds to solid variables to distinguish the fluid and solid domains.

In the fluid field calculations, the velocity $\mathbf{v}$ and the pressure p are the unknown variables; the solid domain calculation involves the nodal displacements $\mathbf{u}^s$, which are defined as the difference of the current and the initial coordinates: $\mathbf{u}^s = \mathbf{x}^s - \mathbf{X}^s$.

To delineate the Lagrangian description for the solid and the Eulerian description for the fluid, we introduce different velocity field variables v_i^s and v_i to represent the motions of the solid in the domain Ω^s and the fluid within the entire domain Ω, respectively. The coupling of these two velocity fields is accomplished with the Dirac delta function

$$v_i^s(\mathbf{X}^s, t) = \int_\Omega v_i(\mathbf{x}, t)\delta(\mathbf{x} - \mathbf{x}^s(\mathbf{X}^s, t))\,\mathrm{d}\Omega. \tag{11}$$

As illustrated in details in [18,11], we define the fluid–structure interaction force within the domain Ω^s as $f_i^{\mathrm{FSI,s}}$, where FSI stands for fluid–structure interaction

$$f_i^{\mathrm{FSI,s}} = -(\rho^s - \rho^f)\frac{\mathrm{d}v_i}{\mathrm{d}t} + \sigma_{ij,j}^s - \sigma_{ij,j}^f + (\rho^s - \rho^f)g_i, \quad \text{in } \Omega^s. \tag{12}$$

The fluid–structure interaction force $f_i^{\mathrm{FSI,s}}$ within the domain Ω^s can be illustrated as the force exerted on the surrounding fluid from the immersed solid.

The cell–cell interaction forces are applied on the surfaces of each cell

$$\sigma_{ij}^s n_j = f_i^c. \tag{13}$$

The transformation of the weak form from the updated Lagrangian to the total Lagrangian description is accomplished by changing the integration domain from Ω^s to Ω_0^s. Since we consider incompressible fluid and solid, the Jacobian determinant is 1 in the solid domain, and the transformation of the weak form to total Lagrangian description yields

$$\int_{\Omega_0^s} \delta u_i(\rho^s - \rho^f)\ddot{u}_i^s\,\mathrm{d}\Omega_0^s + \int_{\Omega_0^s} \delta u_{i,j}P_{ij}\,\mathrm{d}\Omega_0^s - \int_{\Gamma_0^s} \delta u_i f_i^c\,\mathrm{d}\Gamma_0^s - \int_{\Omega_0^s} \delta u_i(\rho^s - \rho^f)g_i\,\mathrm{d}\Omega_0^s + \int_{\Omega_0^s} \delta u_i f_i^{\mathrm{FSI,s}}\,\mathrm{d}\Omega_0^s = 0, \tag{14}$$

where the first Piola–Kirchhoff stress P_{ij} is defined as $P_{ij} := JF_{ik}^{-1}\sigma_{kj}^s$ and the deformation gradient F_{ij} as $F_{ij} := \partial x_i/\partial X_j$.

With respect to the cell–cell interaction force, as shown in Fig. 1, the cut-off length is chosen as 0.5 μm, beyond which the attractive force decays very quickly. In the actual implementation, after the finite element discretization of the solid domain, a sphere with the diameter of the cut-off length is used to identify the cell surface $\mathbf{Y}^c$ within the domain of influence around the cell surface $\mathbf{X}^c$. Hence, the cell–cell interaction force can be denoted as

$$\mathbf{f}^c(\mathbf{X}^c) = -\int_{\Gamma(\mathbf{Y}^c)} \frac{\partial\phi(r)}{\partial r}\frac{\mathbf{r}}{r}\mathrm{d}\Gamma, \tag{15}$$

where $\mathbf{r} = \mathbf{X}^c - \mathbf{Y}^c$, $r = \|\mathbf{X}^c - \mathbf{Y}^c\|$, and $\Gamma(\mathbf{Y}^c)$ represents the cell surface area within the domain of influence surrounding surface $\mathbf{X}^c$.

The symbol $\mathbf{f}^c$ represents the cell–cell interaction force at a surface point exerted by the surfaces of other cells nearby, which has unit of force per unit area. Naturally, the interaction force $f_i^{\mathrm{FSI,s}}$ in Eq. (12) is calculated with the Lagrangian description. Moreover, a Dirac delta function δ is used to distribute the interaction force from the solid domain onto the computational fluid domain Ω

$$f_i^{\mathrm{FSI}}(\mathbf{x}, t) = \int_{\Omega^s} f_i^{\mathrm{FSI,s}}(\mathbf{X}^s, t)\delta(\mathbf{x} - \mathbf{x}^s(\mathbf{X}^s, t))\,\mathrm{d}\Omega. \tag{16}$$

Hence, the equivalent governing equation for the fluid is derived by combining the fluid terms and the interaction force as

$$\rho^{\mathrm{f}} \frac{\mathrm{d}v_i}{\mathrm{d}t} = \sigma^{\mathrm{f}}_{ij,j} + f_{\mathrm{i}}^{\mathrm{FSI}}, \quad \text{in } \Omega. \tag{17}$$

The nonlinear system of equations (17) are solved with the standard stabilized Galerkin method and the Newton–Raphson solution technique [19–21]. To improve the computational efficiency, we also employ the GMRES iterative algorithm and compute the residuals based on matrix-free techniques [22,23].

In particular, we implemented the meshfree reproducing kernel particle method (RKPM) [24–31] for the solid instead of the finite element method used in [11,10], to handle the large deformation of RBCs. The higher order smoothness and larger influence domain of the RKPM shape function provide considerable advantages over the conventional finite element methods in solving large structural deformation problems.

Finally, by approximating the Dirac delta function with the RKPM shape functions, Eq. (11) can be written as

$$v^{\mathrm{s}}_{iI} = \sum_J v_{iJ}(t)\psi_J(\mathbf{x}_J - \mathbf{x}^{\mathrm{s}}_I), \quad \mathbf{x}_J \in \Omega_{\psi_I}, \tag{18}$$

where the discretized delta function ψ_J (an approximation of δ in Eq. (11) is the kernel function introduced in the RKPM.

Here, the solid velocity $\mathbf{v}^{\mathrm{s}}_I$ at node I can be calculated by gathering the velocities at fluid nodes within the domain of influence Ω_{ψ_I}. A dual procedure takes place in the distribution process from the solid onto the fluid grid. The discretized form of Eq. (16) is expressed as

$$f^{\mathrm{FSI}}_{\mathrm{i}J} = \sum_I f^{\mathrm{FSI,s}}_{\mathrm{i}I}(t)\psi_I(\mathbf{x}_J - \mathbf{x}^{\mathrm{s}}_I), \quad \mathbf{x}^{\mathrm{s}}_I \in \Omega_{\psi J}. \tag{19}$$

By interpolating the fluid velocities onto the solid particles in Eq. (18), the fluid within the solid domain is bounded to solid material points. This ensures that not only the no-slip boundary condition on the surface of the solid, but also automatically prevents the fluid from penetrating the solid. The incompressibility of the fluid and Eq. (18) ensure incompressibility, thus volume conservation, of the solid.

3. Results and discussions

The mechanical properties and functions of blood flows are strongly influenced by complex multiscale and multiphysics factors, four of which, namely cell–cell interaction forces, flow shear rates, cell deformability, and vessel geometry will be examined with the proposed numerical procedures. In this section, three multiscale effects in blood rheology are considered in order: the shear rate dependent blood viscosity, the influence of cell rigidity on blood rheology, and the Fahraeus–Lindqvist effect.

3.1. Peeling force of a RBC rouleau

To verify the various ways of RBC rouleau dispersion, several test cases are conducted. First, a RBC adhered to a flat surface under pure shear is tested, where rotation of the RBC rouleau is prohibited. In this case, the RBC has to slide on the adhesive surface. Since the contact surface in this case is quite large, it takes a large force or energy to overcome the adhesion effect and break the rouleau, as shown in Fig. 2.

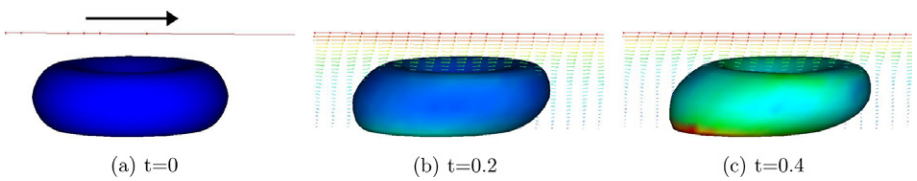

Fig. 2. Pure shear test of a single RBC at the shear rate of 3.0 s^{-1} by applying a shear velocity at the top boundary of the fluid domain. The bottom of the RBC is adhered to a flat surface, thus rotation of the RBC is prohibited. The shear stress is distributed smoothly over the whole cell.

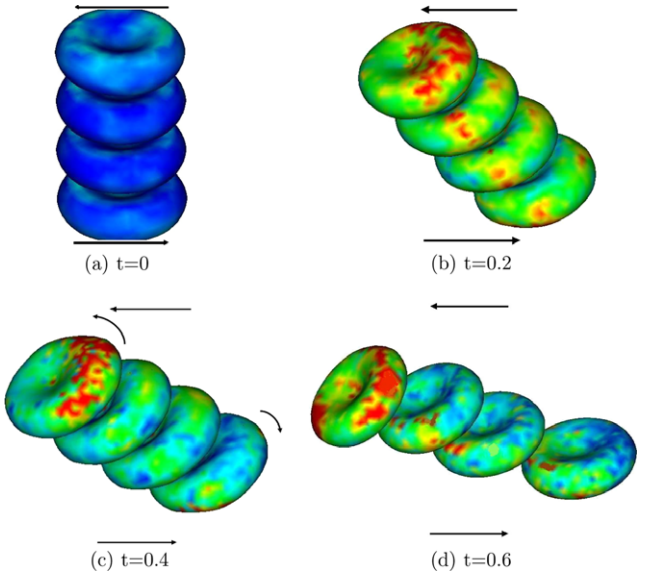

Fig. 3. 'Shear with rotation' test of a RBC rouleau at the shear rate of 3.0 s^{-1}. The shear stress is localized at the peeling edges, indicated by the dark color.

However, if the RBC rouleau is allowed to rotate, which actually occurs in normal shear tests, the RBC rouleau will rotate first and then the RBCs peel away from the rouleau, as indicated in Fig. 3. Since the contact surface during the peeling is much smaller than sliding, and the energy required for peeling off two adhesive surfaces is lower that in sliding, hence it is much easier for RBCs to peel off rather than slide on each other. As indicated in Fig. 3, when peeling occurs, the shear stress is concentrated on the peeling contact area, which will peel off locally and initiate further break up. Yet, another way is to directly pull the rouleau apart along the central axis, which has to resist the adhesive forces. It has been found in this test case that the rotation of RBC rouleau will make it much easier to peel the rouleau apart.

3.2. Shear-rate dependent viscosity

The formation or dispersion of the RBC rouleau depends on the flow condition, the hematocrit of the blood, the fibrinogen density, etc. Here, we focus on the influence of flow condition and hematocrit (RBC volumetric concentration). It is expected that the lower the shear rate (e.g., the slower the blood velocity), the larger in size and denser in number are the RBC aggregates. As the shear rate drops to zero, it is anticipated that human blood becomes one big aggregate, which behaves like a viscoelastic solid. On the contrary, as the shear rate increases, RBC rouleau tends to break up. Individual RBCs also deform, elongate, and align with the streamlines. The deformability and the decrease of cell–cell interaction forces combine to reduce blood viscosity with the increase of the shear rate. As shear rate increases above a certain level (usually 20 s^{-1}), the blood behaves like a Newtonian fluid with a nearly constant viscosity. For rigid particles such as hardened red cells and normal leukocytes, bulk viscosity is essentially independent of the shear rate.

To study the effects of cell aggregation on hemorheology, we put various numbers of RBCs under a shear flow with different shear rates. The fluid domain is a rectangular box with dimensions of $32 \times 20 \times 10$ μm. The diameter of the RBCs is 10 μm. RBCs are placed in the middle of the fluid domain with vertical center–center distance of 3.96 μm. Due to the biconcave shape, the adhesive/repulsive forces mainly exist around the perimeter of the RBCs. The properties for both fluid and a single RBC as well as the discretization for each mesh are summarized in Table 1.

Table 1
Properties of fluid and RBC used for the shear test

Fluid	88,200 nodes 81,792 elements	$\rho^f = 1$ g/cm^3 $\mu = 0.01$ g cm/s	
RBC	1743 nodes 8016 elements	$\rho^s = 1$ g/cm^3 $D = 10$ μm	$C_1 = 2.57 \times 10^6$ dyn/cm^2 $C_2 = 0.257 \times 10^6$ dyn/cm^2

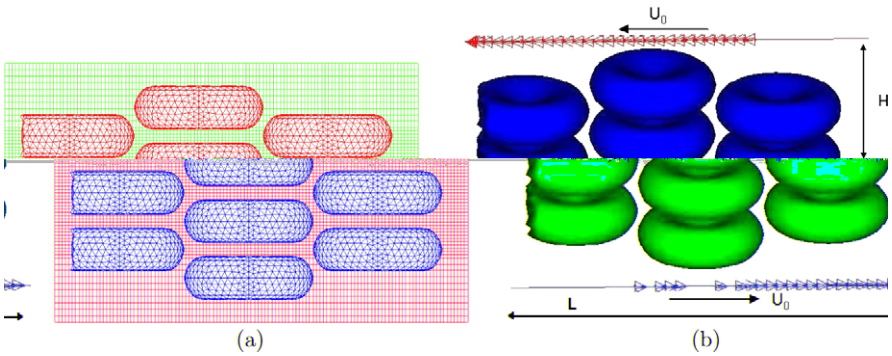

Fig. 4. (a) Mesh for shear of 10 RBCs. (b) Geometry for shear test to calculate viscosity.

As illustrated in Fig. 4, a finer mesh is used in the regions of interest, i.e., in center of the shear plane. A finer mesh provides higher accuracy for these regions with complex flow conditions. The use of a nonuniform fluid mesh is a unique ability and advantage of IFEM over the IB method [16].

The effective viscosity of the blood is calculated from our simulation by measuring the shear force exerted by the plasma onto the shear velocity boundary. The initial geometry of the shear simulation is plotted in Fig. 4(b). A shear velocity of $-U_0$ and $+U_0$ are applied on the top and bottom boundary separately. The fluid domain has a height of $2H$ and a length of L. As an example, by applying a boundary shear velocity of 5 μm/s for both top and bottom surfaces, a shear flow with a rate of 0.5 s^{-1} is obtained in our simulation.

Periodic boundary conditions are used for the left and right boundary (i.e., the RBCs that move out off the left boundary re-enter through the right boundary). The implementation of periodic boundary conditions for the deformable RBCs involves several changes in the calculation. Basically, solid nodes that move out of the right boundary re-enter from the left boundary. The connectivity of the nodes remains. In addition, the delta function, RBC nodal position update, and the deformation gradient calculation are corrected for the periodic boundary.

Without suspending RBCs, the flow velocity in the x direction is given by $u = U_0 y/H$ and the shear force per unit width on the top and bottom walls are given by $F = \mu L U_0/H$. With suspended RBCs, the effective viscosity of the blood is defined as

$$\mu_{\text{eff}} = \frac{HF}{LU_0}. \tag{20}$$

To check the influence of mesh size on our simulation, the effective viscosity of a 10 RBCs cluster under a shear rate of 0.5 s^{-1} is measured by using four sets of fluid meshes with decreasing mesh size. The solid mesh is found to have almost no influence on simulation results with number of nodes above 1000, thus a solid mesh with 1743 nodes and 8016 elements are used through out our simulations. The calculated effective viscosity for

Table 2
Calculated effective viscosity at 0.5 s^{-1} for different fluid mesh sets

Number of nodes	172,081	88,200	52,521	17,220
Number of elements	162,000	81,792	48,000	15,120
μ_{eff} (poise)	0.126	0.124	0.117	0.088

different fluid mesh sets are listed in Table 2. For a set of fluid mesh with 88,200 nodes and 81,792 elements, an effective viscosity of 0.124 poise is obtained, which is within 2% of the value given by the finest mesh with 172,081 nodes and 162,000 elements. Thus, we choose this set of mesh for our shear simulations for reasonable accuracy and efficiency. A time step of 0.001 s is chosen in our simulation and it takes around one minute in a PC with 2.0 GHz CPU.

In a set of numerical experiments, we subject RBC aggregates to a shear flow with different shear rates. First, we put 6 RBCs (corresponds to a hematocrit around 20%) in shear flows with shear rates of 0.25 s^{-1}, 0.5 s^{-1}, and 3.0 s^{-1}, respectively. It is observed that at low shear rate of 0.25 s^{-1}, RBC aggregate rotates as a bulk, as shown in Fig. 5. The cell–cell interaction forces will restrain the disintegration of RBC aggregates and introduce elasticity in the blood's macroscopic mechanical behavior. With the intermediate shear rate, our numerical simulation demonstrates that after the initial rotations, the RBC aggregate aligns with the shear direction and then begins to disaggregate as shown in Fig. 6. At even higher shear rate, the RBC aggregate completely disintegrates and the cells begin to orient themselves into parallel layers as shown in Fig. 7. As evidence of good numerical resolution of the proposed combination of the immersed finite element method and cell interactions, the fluid vorticities surrounding the deformable cells are clearly captured along with the large structural motions and deformations.

The change of adhesion energy during different shear processes is plotted in Fig. 8. It is shown that the adhesion energy first increases, corresponding to the rotation of the rouleau as a whole, then, has a sudden decay due to the peel off of the membranes, and finally goes to zero if completely peeled off. However, for low shear rates, the adhesion energy will fluctuate slowly and remain almost constant, corresponding to the rotation of the rouleau as a whole. The disintegration of RBC aggregates with the increase of the shear rate is an indication of the decrease of the macroscopic viscosity. This is consistent with the experimental observation of Chien [1].

To achieve a RBC concentration close to the hematocrit of human blood, we put 10 RBCs in the same fluid domain, corresponding to a hematocrit around 33%. We put this 10 RBCs cluster under shear flows with different shear rates and measured the effective viscosity as described in Eq. (20). The snap shots of simulations at the shear rate of 0.25 s^{-1}, 0.5 s^{-1}, and 2.0 s^{-1} are shown in Figs. 9–11. As can be seen in these figures, the

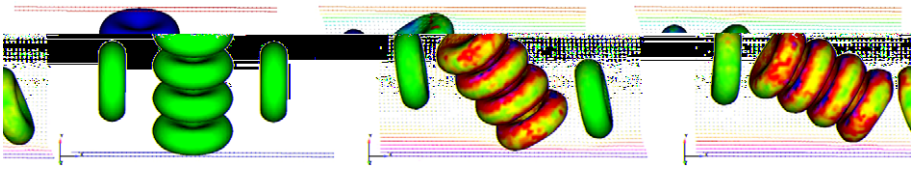

Fig. 5. The shear of the 6-RBC model at the shear rate of 0.25 s^{-1} with cell–cell interaction forces, at $t = 0$ s, $t = 2$ s, and $t = 4$ s.

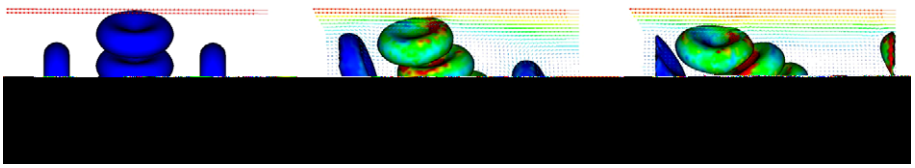

Fig. 6. The shear of the 6-RBC model at the shear rate of 0.5 s^{-1} with cell–cell interaction forces, at $t = 0$ s, t

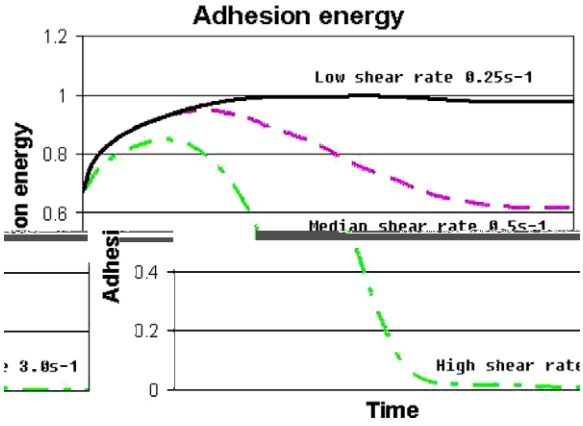

Fig. 8. The adhesion energy change over time for different shear rates.

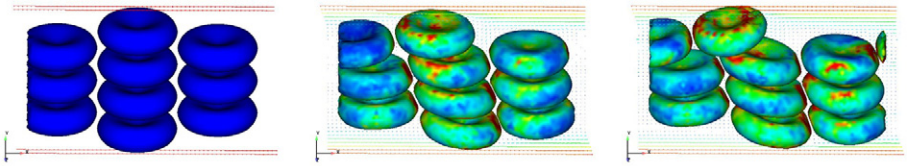

(a) t=0 (b) t=4.8 (c) t=9.6

Fig. 9. The shear of the 10-RBC model with the shear rate of 0.25 s^{-1}.

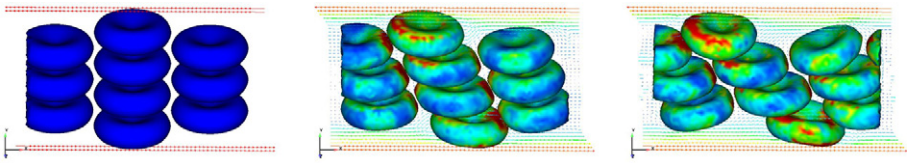

(a) t=0 (b) t=2.4 (c) t=4.8

Fig. 10. The shear of the 10-RBC model with the shear rate of 0.5 s^{-1}.

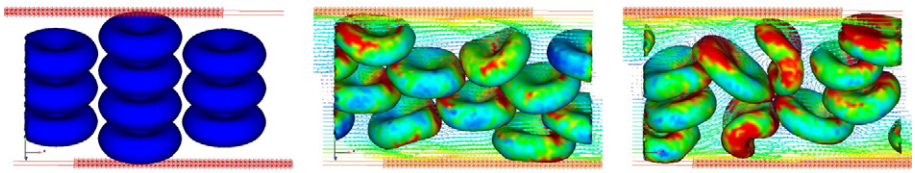

(a) t=0 (b) t=0.6 (c) t=1.2

Fig. 11. The shear of the 10-RBC model with the shear rate of 2.0 s^{-1}.

RBCs experience larger deformation and are more discrete as the shear rate increases. It was found that shear influences RBC aggregation in two different ways. Moderate shear rates from 0.05 s^{-1} to 0.5 s^{-1} facilitates aggregation by increasing RBC encounter, whereas high shear rate above 0.5 s^{-1} causes dispersion of aggregates. A high shear rate flow induces the RBC aggregate to rotate first, then partially disintegrate and eventually align the cells into parallel layers of RBCs as shown in Fig. 11. The effective viscosities of the blood at shear rates between 0.125 s^{-1} and 24 s^{-1} are plotted in Fig. 12. The calculated effective viscosity versus shear-

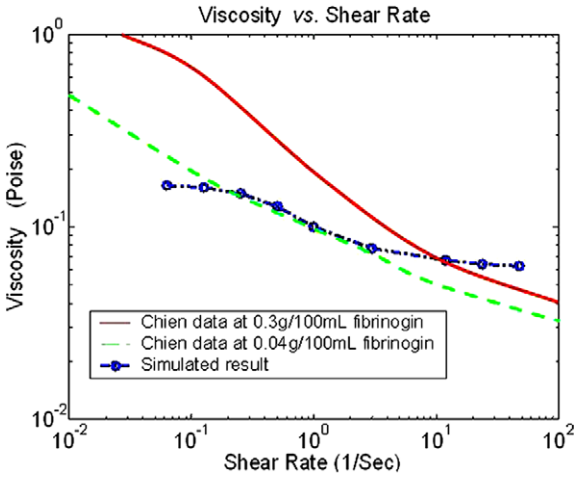

Fig. 12. The effective viscosities of blood at different shear rates. The experimental data is reproduced from [32]. The viscosity measured in [32] is for RBCs at 45% hematocrit in serum with 0.3 g/100 ml and 0.04 g/100 ml fibrinogen.

rate plot qualitatively agrees with the experimental results by Chien et al. [32]. There is a large drop on the viscosity between the shear rates of 0.5 s^{-1} and 3.0 s^{-1}, indicating the dispersion of RBC rouleaus. The effective viscosity changes very slowly for shear rate below 0.125 s^{-1} or above 24 s^{-1}, indicating massive aggregation of RBCs and parallel dispersion of RBCs separately. A precise comparison to the experimental results, however, is hindered by the limited domain size and number of RBCs used in the simulation as well as other complex biochemical factors involved in real blood that is not included in our cell–cell interaction model, and will be addressed in our future works. Yet, to our knowledge, this is the first paper that use direct numerical simulation to link the microscopic mechanism of RBC aggregation to the macroscopic blood viscosity.

3.3. Effect of RBC deformability

To study the effect of the deformability of RBCs on blood viscosity, blood flows with rigid, normal and soft RBCs are simulated separately. The effective viscosity of a dilute suspension of rigid spheres is given by Einstein as

$$\mu_{\text{eff}} = \mu(1 + 2.5\phi), \tag{21}$$

where μ is the viscosity of the suspending fluid and ϕ is the volume fraction of the solid phase ($\phi \approx 0.3$ in our simulation). However, there is no theory that predicts the effective viscosity of a suspension of soft spheres such as RBCs due to the complex nature of the interactions between soft spheres. In this sense, it is valuable to see how the effective viscosity will change if we replace the hardened spheres with soft spheres.

RBCs of different deformability are put under a shear flow of 2.5 s^{-1}. The stiffness of the RBCs decreases five times from hardened ($C_1 = 12.85 \times 10^6$ dyn/cm^2, $C_2 = 1.285 \times 10^6$ dyn/cm^2) to normal ($C_1 = 2.57 \times 10^6$ dyn/cm^2, $C_2 = 0.257 \times 10^6$ dyn/cm^2), and from normal to soft cases ($C_1 = 0.514 \times 10^6$ dyn/cm^2, $C_2 = 0.0514 \times 10^6$ dyn/cm^2).

As can be seen in Fig. 16, the effective viscosity varies greatly as the shear flow develops. This is due to the aggregations formed during the shearing that impedes the flow. The periodic formation and break up of the cell aggregations leads to wide variations in the effective viscosity. Another interesting phenomenon is that the variations in effective viscosity are smaller for soft cells compared to rigid cells. This is due to the fact that it is easier for the soft cells to deform and squeeze through the gaps between each other, while rigid cells are limited by their relative lack of flexibility. This phenomenon is clearly illustrated in Figs. 13–15, where the rigid cells are pushing toward each other while the soft cells squeeze smoothly.

The effective viscosities of the blood for cells of different deformability are plotted in Fig. 17. The calculated effective viscosity increases with the increasing stiffness of the cells. However, Fig. 17 reveals that the

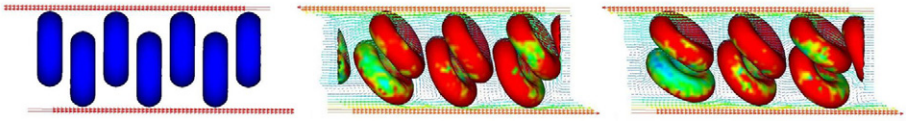

Fig. 13. The shear of 7 RBCs with low deformability at the shear rate of 2.5 s^{-1}, at $t = 0$ s, $t = 0.5$ s, and $t = 1.0$ s.

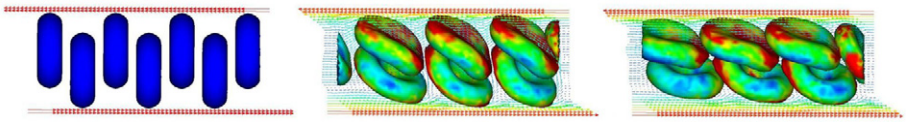

Fig. 14. The shear of 7 RBCs with medium deformability at the shear rate of 2.5 s^{-1}, at $t = 0$ s, $t = 0.5$ s, and $t = 1.0$ s.

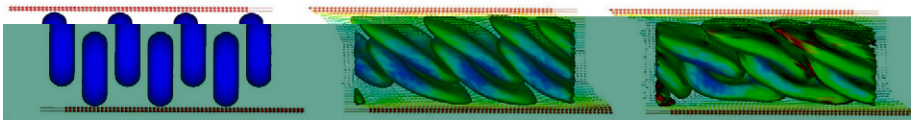

Fig. 15. The shear of 7 RBCs with high deformability at the shear rate of 2.5 s^{-1}, at $t = 0$ s, $t = 0.5$ s, and $t = 1.0$ s.

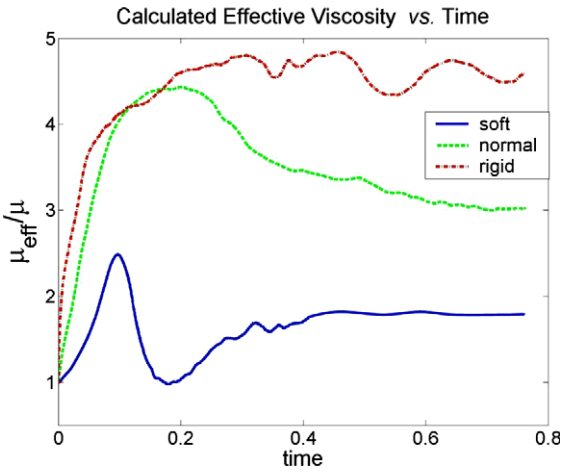

Fig. 16. The calculated effective viscosity vs. time for the shear test of 7 RBCs.

relationship between the stiffness of the cells and the effective viscosity is not linear, but close to exponential. The increase in blood viscosity is observed for blood with sickle cells, which are stiffer than normal RBCs, and is an indication of a disease called sickle cell anemia.

3.4. Fahraeus–Lindqvist effect

It is observed from experiments that the viscosity of blood in narrow tubes is substantially lower than the bulk viscosity. This viscosity increases with the increase in tube diameter, and approaches an asymptotic value for tube diameters larger than 0.3 mm. Such tube diameter dependent viscosity of blood is referred to as the Fahraeus–Lindqvist effect. A physical explanation of this effect is detailed below. The parabolic velocity profile of the capillary flow will lead to the spin of the deformable cells. Due to the spin of deformable RBCs, they tend to migrate toward the center axis of the capillary and hence, a pure plasma region without RBCs, refereed

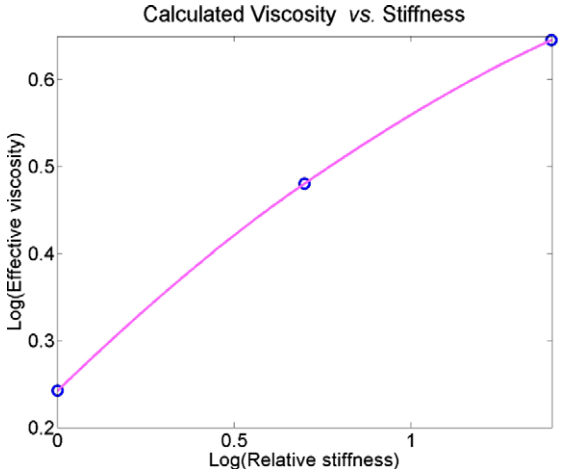

Fig. 17. The calculated effective viscosities of the blood for cell with different deformability.

as the plasma skimming layer, is formed close the wall. As the tube diameter decreases, the area of cross-section of the plasma skimming layer is comparable to the central core. The lower viscosity of the cell free zone will reduce the whole blood viscosity. The smaller the tube diameter, the larger ratio of plasma skimming region to whole tube, leading to a smaller viscosity.

For Newtonian flow through a tube with circular cross-section, the Hagen–Poiseuille solution gives the pressure drop per unit length as

$$\frac{\Delta p}{\Delta L} = \frac{8\mu Q}{\pi r^4}, \tag{22}$$

where μ is the viscosity of the fluid, r is the radius of the tube, L is the length of the tube, and Q is the volume rate of the flow. Since blood is a non-Newtonian fluid, Eq. (22) does not hold anymore, and the apparent viscosity can be defined by measuring $\Delta p/\Delta L$ and Q

$$\mu_{\text{app}} = \frac{\Delta p}{\Delta L}\frac{\pi r^4}{8Q}. \tag{23}$$

Let μ_0 denote the plasma viscosity, the relative viscosity is μ_{app}/μ_0.

We designed a set of simulations of blood flow through tubes with different diameters to capture the Fahraeus–Lindqvist effect. RBCs are aligned vertically inside a tube with increasing diameters from 11 μm to 30 μm. The number of RBCs increases from 3 to 24 to maintain a hematocrit close to 20%. An inflow with an average velocity of 10 μm/s is used to drive the flow from left to the right. The flow velocity at side surface of the tube is fixed at zero, thus enforcing a non-slip boundary condition. The pressure drop per length is

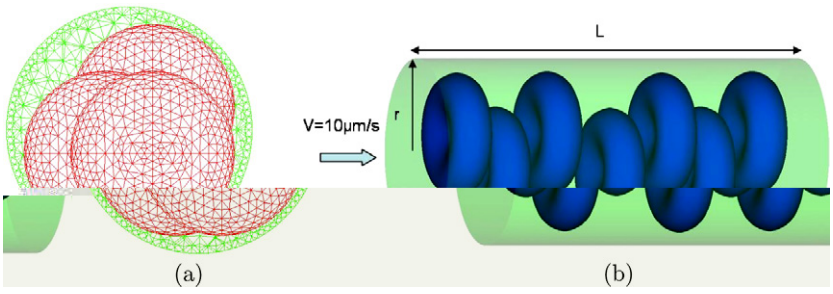

Fig. 18. (a) Mesh for RBCs flow in a tube. (b) Geometry for calculation of apparent viscosity of RBCs flow in a tube.

Table 3
RBCs flow through tubes with different diameters

Tube diameter (μm)	11	15	20	30
Number of RBCs	3	7	12	24
Number of fluid nodes	25,098	27,086	33,360	75,678
Number of fluid elements	121,072	130,811	177,688	415,060

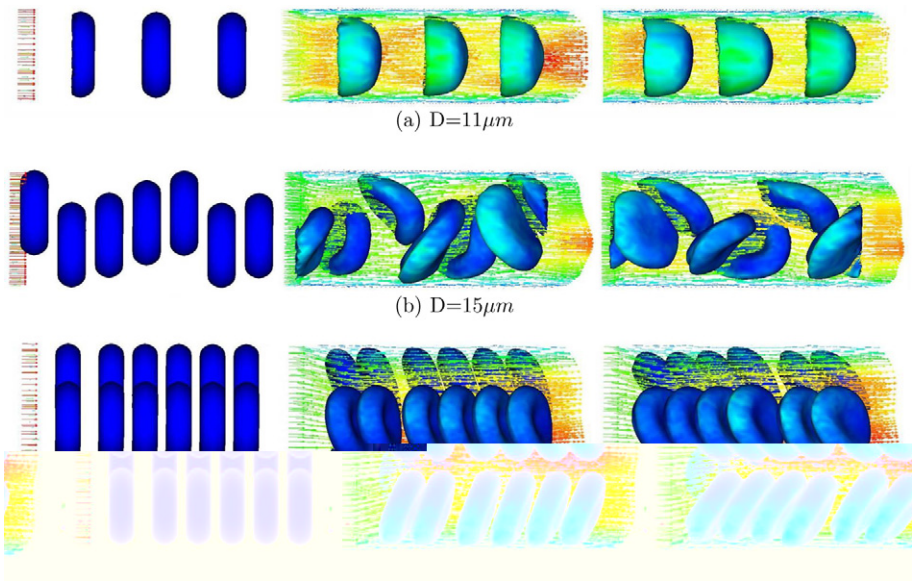

Fig. 19. RBCs flow through a tube with different diameters, at $t = 0$ s, $t = 2.0$ s, and $t = 4.0$ s.

measured as the pressure difference at the inlet and outlet surfaces divided by the tube length. The mesh and geometry used for the 7 RBCs flow in a 15 μm tube are plotted in Fig 18. A finer mesh is used close to the tube surface to resolve the boundary flow. The configurations for RBCs flow in tube with different diameters are listed in Table 3.

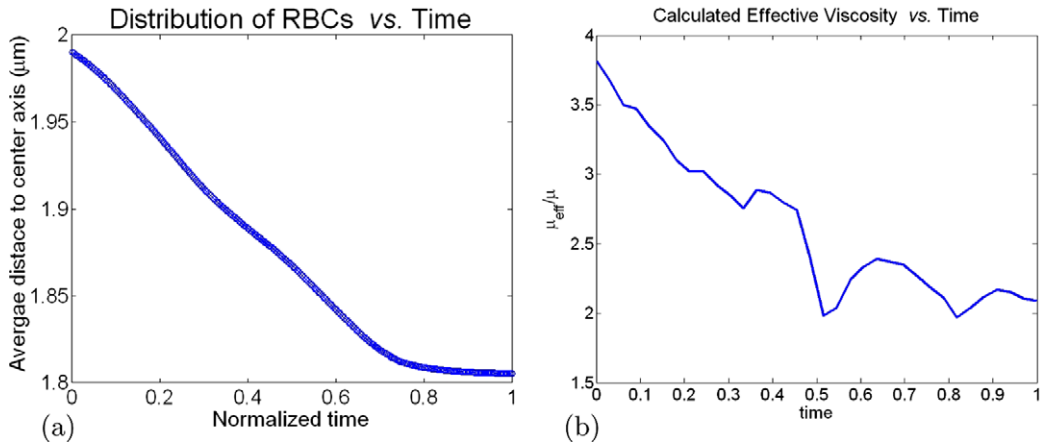

Fig. 20. (a) The radial distribution of the 7 RBCs along a tube with 15 μm diameter. The radial average distance is defined as the average distance from each cell center to capillary center axis. (b) The effective viscosity change over time.

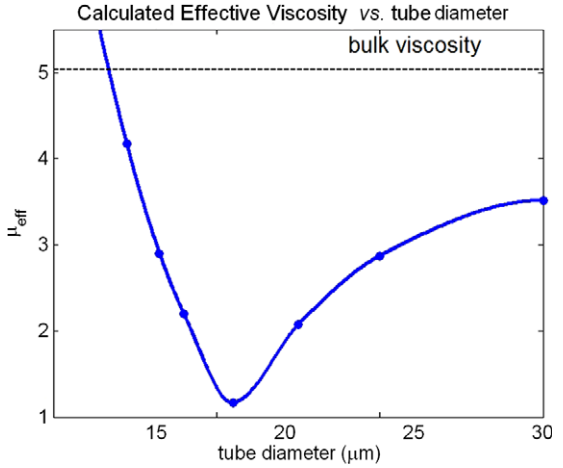

Fig. 21. The effective viscosity of blood flow through tubes of increasing diameters.

The figures of simulations of RBCs flow through tubes of various sizes are shown in Fig. 19. The spin/deformation of the RBCs and the formation of the cell-free zone are accurately captured in our simulation, as presented in Fig. 19. To quantitatively measure the migration of cells toward the tube center, a parameter, the radial average distance of cells, is defined as the average distance from each cell center to capillary center axis. From Fig. 20(a), the radial average distance of cells is decreasing over the time, and hence and more RBCs are concentrated at the tube center. The effective viscosity of the blood is also decreasing over time, as shown in Fig. 20(b), since the cell free region near the capillary wall acts like a lubricative layer. A plot of the effective viscosity of blood flow through tubes with increasing radius is shown in Fig. 21. As it can be seen, the effective viscosity for blood flow through small tubes are much smaller than the bulk blood viscosity. It also shows that the effective viscosity increases as the diameter of the tube increases. It is reported from the experiments that the effective viscosity reached a flatten region marking the effective viscosity of bulk blood when the diameter of the tube is around 0.3 mm. As the diameter of the tube becomes smaller than 10 μm, the effective viscosity increases since the RBCs will block the flow under such small capillary, leading to an increase in apparent viscosity.

4. Conclusions

The coupling of the Navier–Stokes equations and cell–cell interaction in the framework of the immersed finite element method and meshfree method provides a unique tool to model complex blood flows with deformable RBCs within micro- and capillary vessels in three dimensions. The microscopic mechanism of RBC aggregation is linked seamlessly to the macroscopic behaviors of the blood, such as the shear rate dependent viscosity of the blood. This is the first attempt to use a multiscale numerical approach to study the rheology of RBC aggregation. The simulated disaggregation of a RBC rouleau at different shear rates clearly explains the effects of shear rates on RBC rouleau break-up. The viscosity of deformable cells is shown to be different from the rigid case that is usually modeled in the literature. The Fahraeus–Lindqvist effect is also clearly illustrated in our simulation.

Acknowledgements

The authors thank NSF for the financial support.

References

[1] S. Chien, Electrochemical interactions between erythrocyte surfaces, Thrombosis Research 8 (1976) 189–202.
[2] E.A. Evans, Y.C. Fung, Improved measurements of the erythrocyte geometry, Microvascular Research 4 (1972) 335.

[3] I. Fontaine, D. Savery, G. Cloutier, Simulation of ultrasound backscattering by red cell aggregates: effect of shear rate and anisotropy, Biophysical Journal 82 (2002) 1696–1710.
[4] B. Neu, H.J. Meiselman, Depletion-mediated red blood cell aggregation in polymer solutions, Biophysical Journal 83 (November) (2002) 2482–2490.
[5] Y. Huang, C.M. Doerschuk, R.D. Kamm, Computational modeling of RBC and neutrophil transit through the pulmonary capillaries, Journal of Applied Physiology 90 (2) (2001) 545–564.
[6] S.L. Diamond, Reaction complexity of flowing human blood, Biophysical Journal 80 (2001) 1031–1032.
[7] C.D. Eggleton, A.S. Popel, Large deformation of red cell ghosts in a simple shear flow, Physics of Fluids 10 (8) (1998) 1834–1845.
[8] G.J. Wagner, N. Moës, W.K. Liu, T.B. Belytschko, The extended finite element method for rigid particles in stokes flow, International Journal for Numerical Methods in Engineering 51 (3) (2001) 293–313.
[9] G.J. Wagner, S. Ghosal, W.K. Liu, Particulate flow simulations using lubrication theory solution enrichment, International Journal for Numerical Methods in Engineering 56 (9) (2003) 1261–1289.
[10] Y. Liu, L. Zhang, X. Wang, W.K. Liu, Coupling of Navier–Stokes equations with protein molecular dynamics and its application to hemodynamics, International Journal for Numerical Methods in Fluids 46 (2004) 1237–1252.
[11] L. Zhang, A. Gerstenberger, X. Wang, W.K. Liu, Immersed finite element method, Computer Methods in Applied Mechanics and Engineering 193 (21–22) (2004) 2051–2067.
[12] R. Skalak, A. Tozeren, R.P. Zarda, S. Chien, Strain energy function of red blood cell membranes, Biophysical Journal 13 (1973) 245–264.
[13] C. Pozrikidis, Numerical simulation of the flow-induced deformation of red blood cells, Annals of Biomedical Engineering 31 (2003) 1–12.
[14] R. Skalak, P.R. Zarda, K.M. Jan, S. Chien, Mechanics of rouleau formation, Biophysical Journal 35 (1981) 771–781.
[15] K. Buxbaum, E. Evans, D. Brooks, Quantitation of surface affinities of red blood cells in dextran solutions and plasma, Biochemistry 21 (1982) 3235–3239.
[16] C.S. Peskin, D.M. McQueen, A three-dimensional computational method for blood flow in the heart. I. Immersed elastic fibers in a viscous incompressible fluid, Journal of Computational Physics 81 (2) (1989) 372–405.
[17] C.S. Peskin, D.M. McQueen, Computational biofluid dynamics, Contemporary Mathematics 141 (1993) 161–186.
[18] X. Wang, W.K. Liu, Extended immersed boundary method using FEM and RKPM, Computer Methods in Applied Mechanics and Engineering 193 (12–14) (2004) 1305–1321.
[19] T.E. Tezduyar, Stabilized finite element formulations for incompressible-flow computations, Advances in Applied Mechanics 28 (1992) 1–44.
[20] T.E. Tezduyar, Finite element methods for flow problems with moving boundaries and interfaces, Archives of Computational Methods in Engineering 8 (2) (2001) 83–130.
[21] T.J.R. Hughes, L.P. Franca, M. Balestra, A new finite element formulation for computational fluid dynamics: V. Circumventing the Babuška–Brezzi condition: a stable Petrov–Galerkin formulation of the Stokes problem accommodating equal-order interpolations, Computer Methods in Applied Mechanics and Engineering 59 (1986) 85–99.
[22] Y. Saad, M.H. Schultz, GMRES: a generalized minimal residual algorithm for solving nonsymmetric linear systems, SIAM Journal on Scientific and Statistical Computing 7 (3) (1986) 856–869.
[23] L. Zhang, G.J. Wagner, W.K. Liu, A parallelized meshfree method with boundary enrichment for large-scale CFD, Journal of Computational Physics 176 (2002) 483–506.
[24] W.K. Liu, S. Jun, Y.F. Zhang, Reproducing kernel particle methods, International Journal for Numerical Methods in Fluids 20 (1995) 1081–1106.
[25] T.B. Belytschko, W.K. Liu, B. Moran, Nonlinear Finite Elements for Continua and Structures, Wiley, New York, 2000.
[26] W.K. Liu, Y. Chen, R.A. Uras, C.T. Chang, Generalized multiple scale reproducing kernel particle methods, Computer Methods in Applied Mechanics and Engineering 139 (1996) 91–158.
[27] S. Li, W.K. Liu, Meshfree and particle methods and their applications, Applied Mechanics Review 55 (2002) 1–34.
[28] S. Li, W.K. Liu, Meshfree Particle Methods, Springer, Berlin, 2004.
[29] W.K. Liu, T.B. Belytschko, H. Chang, An arbitrary Lagrangian–Eulerian finite element method for path-dependent materials, Computer Methods in Applied Mechanics and Engineering 58 (1986) 227–245.
[30] W.K. Liu, H. Chang, J. Chen, T.B. Belytschko, Arbitrary Lagrangian–Eulerian Petrov–Galerkin finite elements for nonlinear continua, Computer Methods in Applied Mechanics and Engineering 68 (1988) 259–310.
[31] W.K. Liu, H. Chang, J. Chen, T. Belytschko, Arbitrary Lagrangian–Eulerian Petrov–Galerkin finite elements for nonlinear continua, Computer Methods in Applied Mechanics and Engineering 68 (3) (1988) 259–310.
[32] S. Chien, S. Usami, R. Dellenback, M. Gregersen, Shear-dependent interaction of plasma proteins with erythrocytes in blood rheology, American Journal of Physiology 219 (1970) 143–153.
[33] D.W. Kim, S.Q. Tang, W.K. Liu, Mathematical foundations of the immersed finite element method, Computational Mechanics (2006) doi:10.1007/s00466-005-0018-5.